

A swirling flare-related EUV jet

Q. M. Zhang and H. S. Ji

Key Laboratory for Dark Matter and Space Science, Purple Mountain Observatory, CAS, Nanjing
210008, China

e-mail: zhangqm@pmo.ac.cn

Received; accepted

ABSTRACT

Aims. We report our observations of a swirling flare-related EUV jet on 2011 October 15 at the edge of NOAA active region 11314.

Methods. We utilised the multiwavelength observations in the extreme-ultraviolet (EUV) passbands from the Atmospheric Imaging Assembly (AIA) aboard the Solar Dynamics Observatory (SDO). We extracted a wide slit along the jet axis and 12 thin slits across its axis to investigate the longitudinal motion and transverse rotation. We also used data from the Extreme-Ultraviolet Imager (EUVI) aboard the Solar TERrestrial RELations Observatory (STEREO) spacecraft to investigate the three-dimensional (3D) structure of the jet. Ground-based $H\alpha$ images from the El Teide as a member of the Global Oscillation Network Group (GONG) provide a good opportunity to explore the relationship between the cool surge and hot jet. Line-of-sight magnetograms from the Helioseismic and Magnetic Imager (HMI) aboard SDO enable us to study the magnetic evolution of the flare/jet event. We carried out potential-field extrapolation to figure out the magnetic configuration associated with the jet.

Results. The onset of jet eruption coincided with the start time of C1.6 flare impulsive phase. The initial velocity and acceleration of the longitudinal motion were $254 \pm 10 \text{ km s}^{-1}$ and $-97 \pm 5 \text{ m s}^{-2}$, respectively. The jet presented helical structure and transverse swirling motion at the beginning of its eruption. The counter-clockwise rotation slowed down from an average velocity of $\sim 122 \text{ km s}^{-1}$ to $\sim 80 \text{ km s}^{-1}$. The interwinding thick threads of the jet untwisted into multiple thin threads during the rotation that lasted for 1 cycle with a period of $\sim 7 \text{ min}$ and an amplitude that increases from $\sim 3.2 \text{ Mm}$ at the bottom to $\sim 11 \text{ Mm}$ at the upper part. Afterwards, the curtain-like leading edge of the jet continued rising without rotation, leaving a dimming region behind before falling back to the solar surface. The appearance/disappearance of dimming corresponded to the longitudinal ascending/descending motions of jet. Cospatial $H\alpha$ surge and EUV dimming imply that the dimming resulted from the absorption of hot EUV emission by cool surge. The flare/jet event was caused by continuous magnetic cancellation before the start of flare. The jet was associated with the open magnetic fields at the edge of AR 11314.

Key words. Sun: corona – Sun: oscillations – Sun: flares

1. Introduction

There are various jet-like activities in the solar atmosphere, such as spicules (De Pontieu et al. 2004), chromospheric jets (Shibata et al. 2007; Nishizuka et al. 2008; Liu et al. 2009, 2011b; Singh

et al. 2012), $H\alpha$ surges (Schmieder et al. 1995; Zhang et al. 2000; Liu & Kurokawa 2004; Jiang et al. 2007), extreme-ultraviolet (EUV) jets (Chae et al. 1999; Nisticò et al. 2009; Moschou et al. 2012), and soft X-ray (SXR) jets (Shibata et al. 1992; Savcheva et al. 2007). Most of the coronal jets seen in EUV and SXR are associated with flares, microflares, or bright points at their footpoints (Ji et al. 2008; Zhang et al. 2012; Zhang & Ji 2013). The typical height of jets is 10–400 Mm, the width is 5–100 Mm, the longitudinal velocity is 10–1000 km s⁻¹ with an average value of ~ 200 km s⁻¹, and the kinetic energy is in the order of 10^{25} – 10^{28} ergs (Shimojo et al. 1996). Coronal jets are formed in coronal holes (Wang et al. 1998; Cirtain et al. 2007; Culhane 2007; Patsourakos et al. 2008) or at the edge of active regions (Kim et al. 2007; Guo et al. 2013) in the presence of open magnetic fields. Particles are accelerated and ejected into the interplanetary space during the reconnection, generating Type III radio bursts (Krucker et al. 2011; Glesener et al. 2012). Coronal jets are believed to be heated by magnetic reconnection between emerging flux and the pre-existing magnetic fields (Yokoyama & Shibata 1996; Moreno-Insertis et al. 2008; Török et al. 2009; Jiang et al. 2012; Moreno-Insertis & Galsgaard 2013; Pontin et al. 2013). Moore et al. (2010) classified jets into two types: standard jets and blowout jets, the later of which features blowout eruption of the base arch’s core field.

Apart from the ordinary collimated motions, jets occasionally exhibit helical structure and untwisting motions (Liu et al. 2011a; Shen et al. 2011; Chen et al. 2012; Hong et al. 2013; Schmieder et al. 2013). The amplitude of transverse rotations ranges from 2 to 10 Mm. The periods are in the order of 4–9 min. The transverse velocities (10–150 km s⁻¹) are slightly lower than their longitudinal velocities along the jet axis. The untwisting motions were previously interpreted as the releasing of magnetic helicity during the reconnection between a twisted bipole and open fields (Shibata & Uchida 1986; Canfield et al. 1996; Jibben & Canfield 2004). Pariat et al. (2009, 2010) numerically simulated the formation of untwisting jets as a result of continuous pumping of magnetic free energy and helicity into the corona from the photosphere, which is interpreted as upward propagation of torsional Alfvén waves at a speed of hundreds of km s⁻¹. Numerous flare-related jets and rotating jets have been observed. In this paper, we report the helical structure and swirling motion of a flare-related EUV jet observed by the Atmospheric Imaging Assembly (AIA; Lemen et al. 2012) aboard the Solar Dynamics Observatory (SDO) spacecraft. In §2, we describe the multiwavelength data analysis. The results are shown in §3. Discussion and summary are presented in §4.

2. Data analysis

SDO/AIA has unprecedentedly high cadence and resolution in the seven EUV wavelengths (94, 131, 171, 193, 211, 304, and 335 Å). A C1.6 flare and the accompanying jet at the edge of NOAA active region 11314 was observed by AIA during 11:00–14:00 UT on 2011 October 15. The full-disk level_1 fits data were calibrated using the standard program *aia_prep.pro* in the *Solar Software*. Image coalignments between the EUV passbands were performed using the cross-correlation method after selecting a bright feature (e.g., active region). The accuracy of coalignments is 1''2. In order to investigate the three-dimensional (3D) structure of the jet, we checked data from the Extreme-Ultraviolet Imager (EUVI) in the Sun Earth Connection Coronal and Heliospheric Investigation (SECCHI; Howard et al. 2008) package aboard the Solar TERrestrial

Table 1. Description of the Observational Parameters

Instrument	λ (Å)	Time (UT)	Cadence (sec)	Pixel Size (arcsec)
AIA	94–335	11:00–14:00	12	0.6
HMI	–	11:00–14:00	45	0.6
EUVI	195	11:00–14:00	300	1.6
El Teide	6563	11:10–11:57	60	1.0
El Teide	6563	13:12–14:00	60	1.0
GOES	0.5–4.0	11:00–14:00	3	–
GOES	1.0–8.0	11:00–14:00	3	–

Relations Observatory (STEREO; Kaiser 2005). The orbits of the twin satellites (A and B) drifted as time goes by, so that they had separation angles of $\sim 105^\circ$ and $\sim 99^\circ$ with the Sun-Earth connection on that day. Combined with SDO, the perspectives from STEREO provide excellent opportunity to get a full-view of solar eruptions. The 195 Å raw data were calibrated by using the program *secchi_prep.pro*. Deviation of the STEREO N-S direction from the solar rotation axis was corrected. After checking the EUV observation during that time, we found that the jet was visible only in the field-of-view of STEREO-B, but still partly blocked by the solar western limb. To explore the relationship between the hot jet and cool surge, we examined the ground-based $H\alpha$ observation from the El Teide as a member of the Global Oscillation Network Group (GONG). The $H\alpha$ images were coaligned with the AIA 304 Å images due to their lower formation heights. Unfortunately, there was a data gap during 11:57–13:12 UT when the flare occurred. The line-of-sight (LOS) magnetograms from the Helioseismic and Magnetic Imager (HMI; Scherrer et al. 2012) aboard SDO were used to study the temporal evolution of magnetic fields in the photosphere. The magnetograms were coaligned with the $H\alpha$ images according to the position of sunspot. Moreover, we carried out potential-field extrapolation to figure out the 3D magnetic configuration of the jet. The E-W and N-S scopes of the magnetogram for extrapolation were $886''.8$ and $706''.2$ so that flux balance was guaranteed. SXR light curves from the GOES spacecraft were utilised to investigate the evolution of C1.6 flare. The observing parameters are summarised in Table 1, including the instruments, wavelengths (λ), observing times, cadences, and pixel sizes.

3. Results

In Fig. 1, the three snapshots of AIA 193 Å images represent the three phases of flare: pre-flare phase (a), impulsive phase (b), and main phase (c), respectively. In the pre-flare phase, there was very weak brightening at the flare site in the absence of jet. In the impulsive phase, the area and total emission of flare quickly increased and reached maximum. The helical structure of jet was composed of two interwinding threads (“T1” and “T2”) that started counter-clockwise rotation perpendicular to its axis. In the main phase, the total emission of flare decreased significantly. The two compact threads untwisted into many thin threads, implying the multistrand nature of jet. Afterwards, the jet experienced curtain-like eruption along its axis. To investigate the longitudinal and transverse motions, we extracted a wide slit along the axis and 12 narrow slits (from cut0 to cut11) perpendicular to the axis in Fig. 1c. The wide slit (solid box) is $12''$ in width and $182''$ in

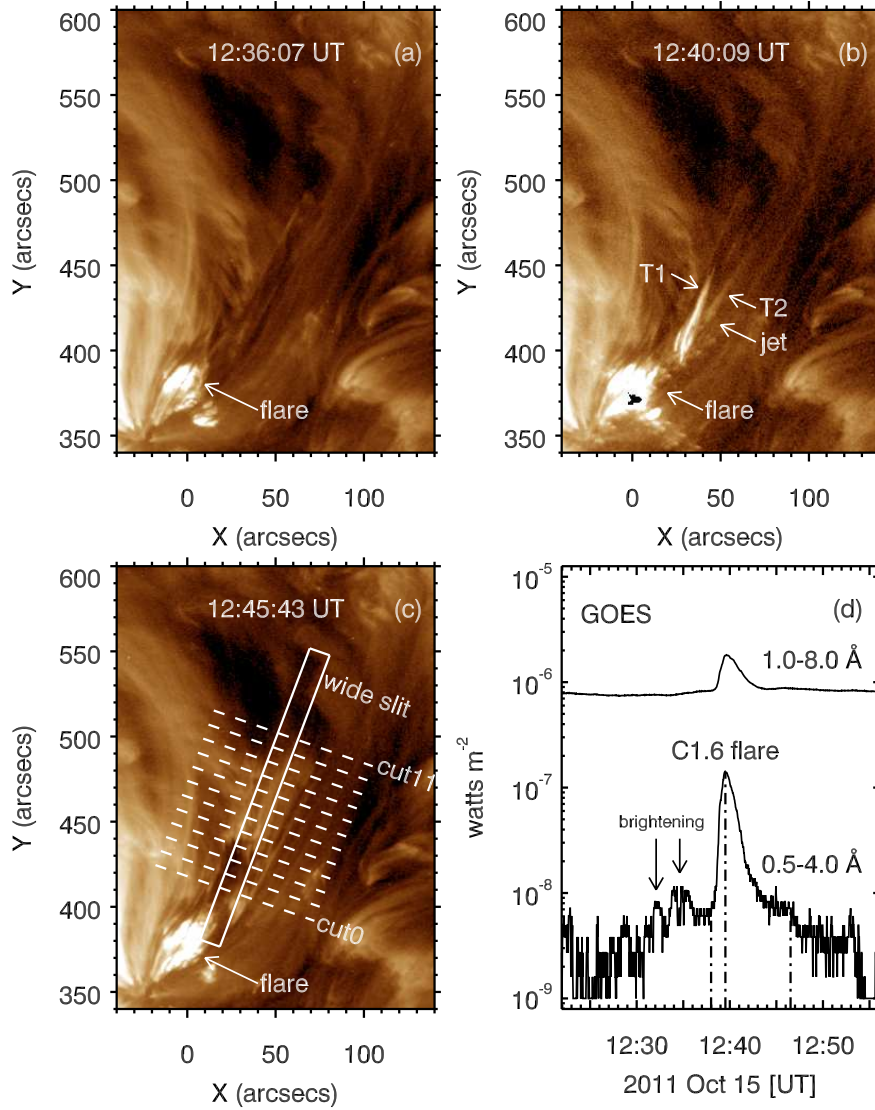


Fig. 1. (a)–(c) Three snapshots of the 193 \AA images. The white arrows point to the flare and jet. In panel (b), the two thick threads of jet are labeled with “T1” and “T2”. In panel (c), the solid box and dashed lines represent the wide slit and 12 narrow slits (cut0–cut11), respectively. (d) GOES light curves in $1-8 \text{ \AA}$ (upper) and $0.5-4.0 \text{ \AA}$ (lower), featuring the C1.6 flare and weak precursor brightenings. The dash-dotted lines denote the start (12:38:00 UT) and peak (12:39:30 UT) of the flare impulsive phase and end (12:46:30 UT) of the main phase. The temporal evolution is shown in a movie with a larger field-of-view available in the online edition.

length. The narrow slits (dashed lines) are $96''$ in length. In Fig. 1d, we plot the light curves in $1.0-8.0 \text{ \AA}$ (upper) and $0.5-4.0 \text{ \AA}$ (lower). The impulsive phase of flare started at 12:38:00 UT and peaked at 12:39:30 UT, and the main phase ended at 12:46:30 UT, which is marked by the dash-dotted lines.

In Fig. 2, the time-slice diagrams of the wide slit in six of the EUV passbands (131, 171, 193, 211, 304, and 335 \AA) illustrate the longitudinal motion of jet along its axis. The jet underwent

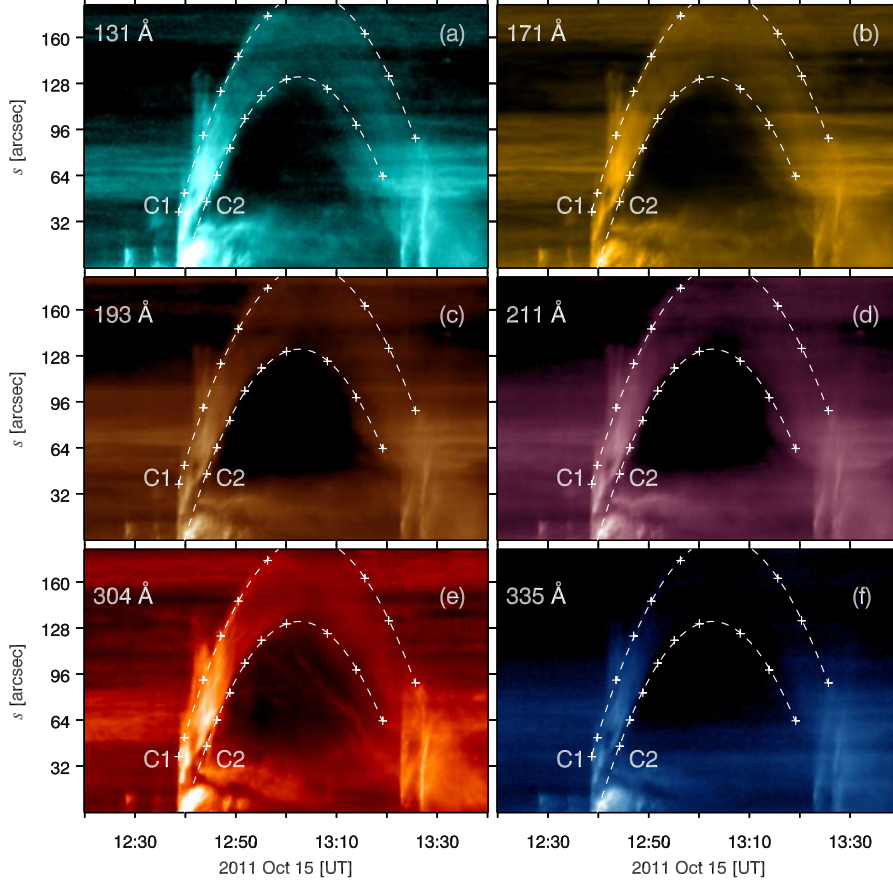


Fig. 2. (a)–(f) Time-slice diagrams of the wide slit in six of the EUV passbands. $s = 0''$ and $182''$ in y -axis represent the bottom-left and top-right endpoints of the slit. The two dashed lines stand for the outer (C1) and inner (C2) boundaries of the parabolic trajectory.

a parabolic trajectory during 12:38–13:25 UT. We outline the outer and inner boundaries of the trajectory with two curves (C1 and C2) that are fitted with a quadratic function:

$$s = s_0 + v_{\parallel}(t - t_0) + \frac{1}{2}g_{\parallel}(t - t_0)^2, \quad (1)$$

where $t_0 = 12:38$ UT, the initial velocity $v_{\parallel} = 264$ and 244 km s^{-1} , the acceleration $g_{\parallel} = -103$ and -92 m s^{-2} for C1 and C2, respectively. Combining the two curves, we obtain $v_{\parallel} = 254 \pm 10$ km s^{-1} and $g_{\parallel} = -97 \pm 5$ m s^{-2} .

Figure 3 displays the time-slice diagrams of 10 narrow slits (cut2–cut11) in 193 \AA . s in y -axis of each panel signifies the distance from the top-left endpoints of slits. The middle of y -axis ($s = 48''$) corresponds to the position of jet axis. It is clear that the jet rotated leftwards during $\sim 12:40$ – $12:44$ UT, which is illustrated by the solid oblique lines whose slopes stand for the transverse velocities. The jet rotated rightwards during $\sim 12:44$ – $12:48$ UT, which is also illustrated by the oblique lines. We calculated the jet velocities from the 34 labeled lines and show the histogram in Fig. 4 where negative/positive values represent leftwards/rightwards rotation. It is revealed that the rotation slowed down from an average leftward speed of ~ 122 km s^{-1} to an average rightward speed of ~ 80 km s^{-1} . The rotation lasted for only 1 cycle whose period (427 s) and twofold amplitude (22 Mm) are marked in the time-slice diagram of cut5, i.e., the seventh row of Fig. 3.

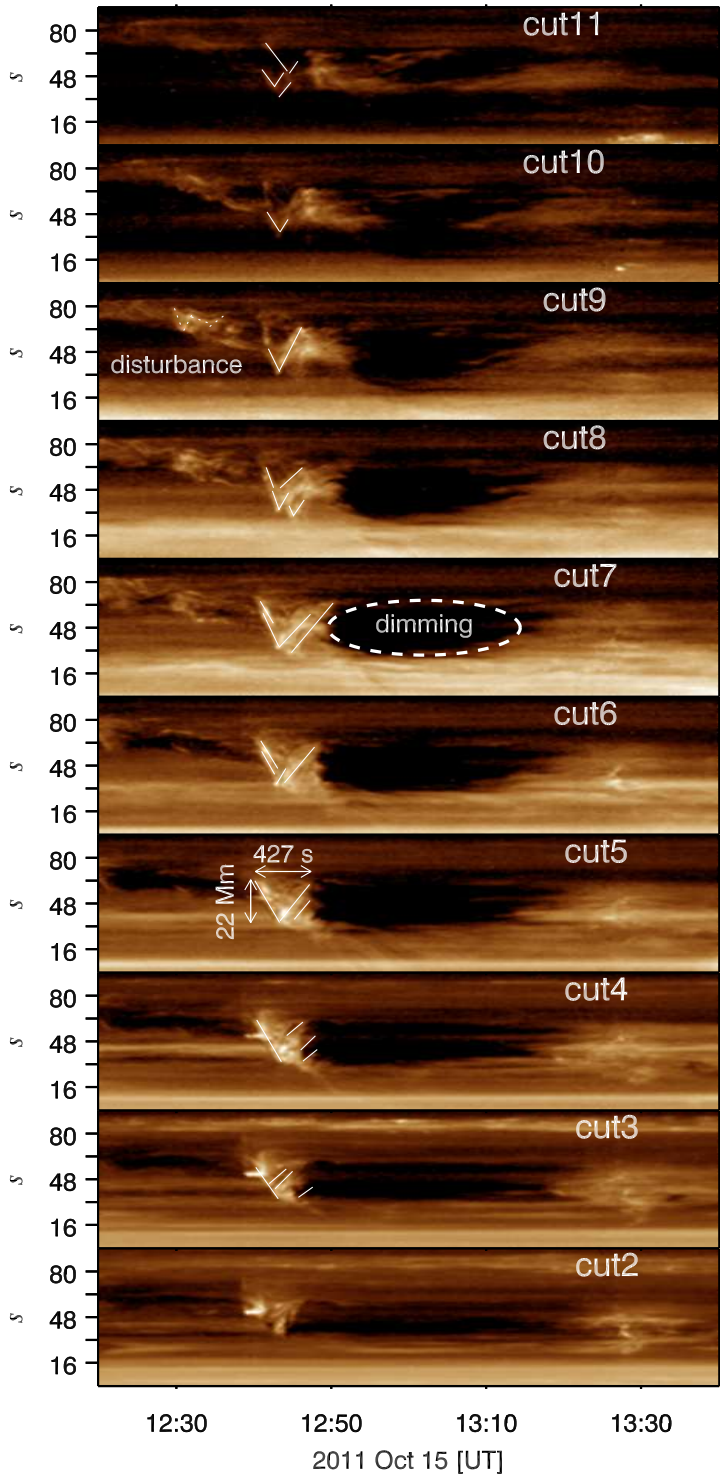


Fig. 3. Time-slice diagrams of the ten narrow slits (cut2–cut11) in 193 \AA . $s = 0''$ and $96''$ in y -axis signify the top-left and bottom-right endpoints of slits. The short solid lines denote the 34 manually selected bright features signifying the leftwards and rightwards transverse rotation of the jet. The short dotted lines in the third row denote the four manually selected bright features signifying the precursor disturbances adjacent to the jet axis. The dashed ellipse in the fifth panel outlines the boundary of dimming. The horizontal and vertical double-headed arrows in the seventh panel measure the period (427 s) and double amplitude (22 Mm) of rotation.

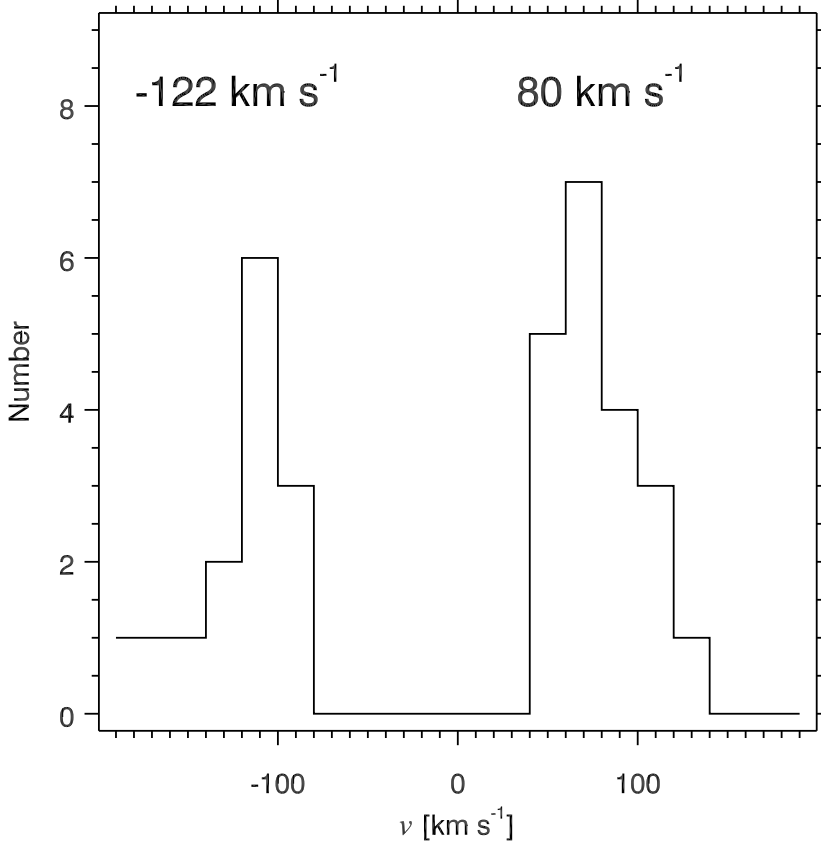


Fig. 4. Histogram of the transverse velocities of jet rotation. Negative/positive values suggest leftwards/rightwards motions. The average leftward speed (-122 km s^{-1}) and average rightward speed (80 km s^{-1}) of the jet rotation are labeled.

The near-simultaneous reversals of direction around 12:44 UT indicate that the whole jet rotated in phase.

After the transverse rotation, the helical jet became curtain-like and continued rising in the longitudinal direction, leaving behind a dimming, which is manifested by the central dark regions in all panels of Fig. 3. We label the dimming region with a dashed ellipse in the fifth row of Fig. 3. The appearances of dimming occurred successively from the lower to upper parts of jet. The disappearances of dimming took place successively, however, from the upper to lower parts of jet. Combining with the longitudinal evolutions of the jet in Fig. 2, we found that the appearance/disappearance of dimming coincided with the longitudinal ascending/descending motions.

Figure 5 shows the time-slice diagram of cut0 that is close to the base of jet. The helical feature in the diagram suggests transverse rotation during $\sim 12:42\text{--}12:55$ UT. According to the handedness of feature, we conclude that the jet rotated counter-clockwise with respect to its axis. We extracted the intensity profile along the center of the helical pattern, which is labeled with a solid line bounded by two dashed lines. The distance (6.4 Mm) between the dashed lines equals to double amplitude of rotation at cut0.

In the left panel of Fig. 6, the intensity profile and its quadratic-fitted trend are plotted in solid and dotted lines. It is evident that the intensity profile presents quasi-periodic oscillation. The result

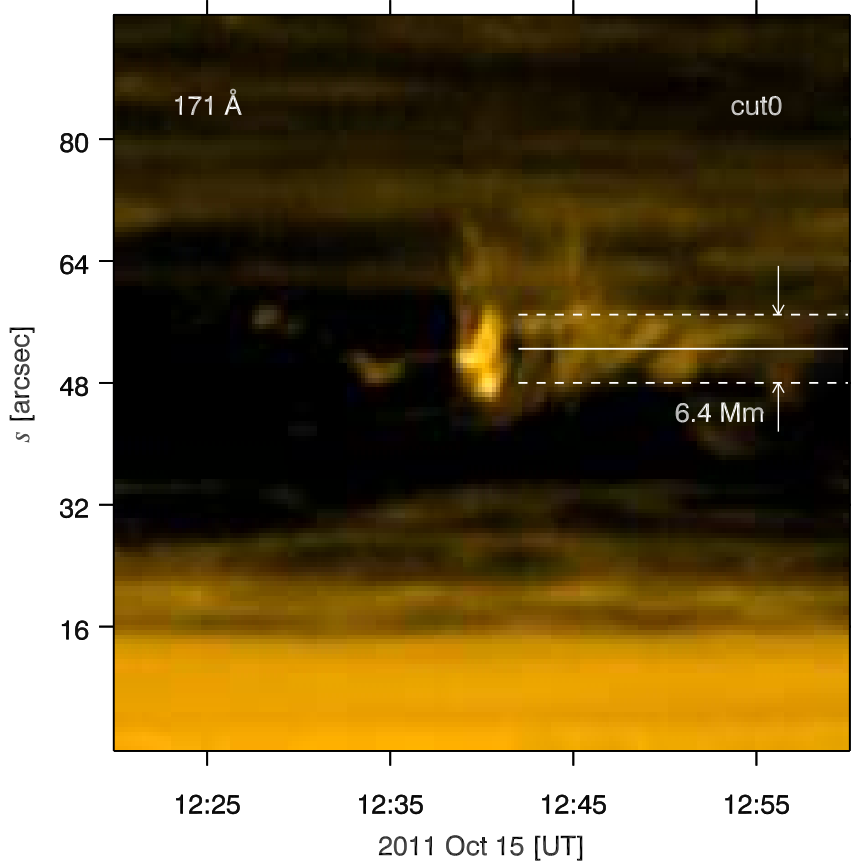


Fig. 5. Time-slice diagram of cut0 near the bottom of jet in 171 \AA . The solid and dashed lines mark the center and boundaries of the helical feature that indicates swirling motion of the jet. The distance between the dashed lines (6.4 Mm) equals to double amplitude of jet rotation at cut0.

of wavelet transform of the trend-removed profile is shown in the right panel where bright yellow region at the center suggests quasi-periodicity of the curve with period of $\sim 192 \text{ s}$. However, considering that the jet was composed of two compact interwinding threads at its bottom (“T1” and “T2” in Fig. 1b), the true period of rotation should be $\sim 384 \text{ s}$, which is slightly shorter than the measured value of 427 s in the seventh panel of Fig. 3, implying that the jet rotates faster at the lower part than the upper part. The amplitude of rotation at the base of jet ($\sim 3.2 \text{ Mm}$) accounts for 30% of the value at the upper part.

Figure 7 shows the $H\alpha$ and AIA 193 \AA images at 13:12 UT. It is clear that the cool surge seen in $H\alpha$ passband is cospatial with the dimming region following the jet leading edge. The surge was visible until 13:17 UT. Unfortunately, there was a data gap before 13:12 UT. We are unable to investigate the temporal relation between the jet and surge during the flare.

The compact solar flare are usually associated with magnetic flux emergence or cancellation. To understand the cause of flare/jet event, we checked the HMI LOS magnetograms. In Fig. 8, we display four magnetograms around the sunspot of AR 11314. The flare took place near the north-west boundary of the strong sunspot with negative magnetic polarity (Fig. 8d). We label the negative-polarity region around the sunspot with “N” (Fig. 8b) and the neighbouring positive-polarity regions with “P1” (Fig. 8a) and “P2” (Fig. 8c). After viewing the movie of magnetograms,

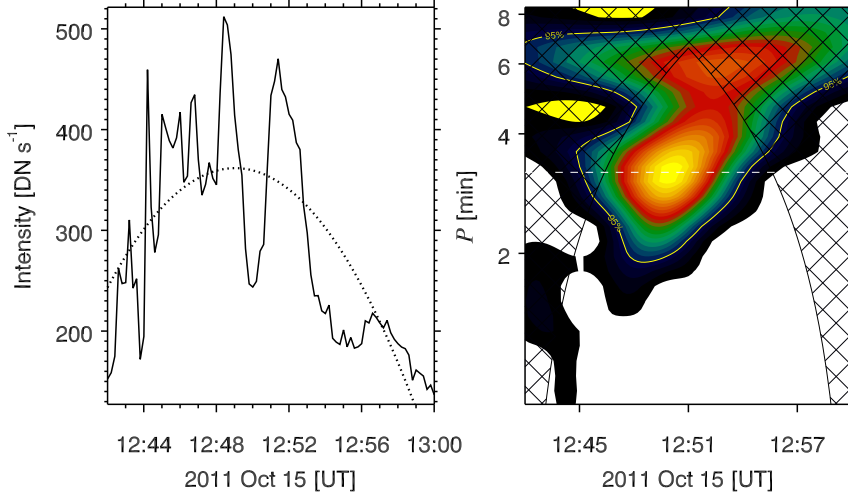


Fig. 6. *Left panel:* Intensity profile (solid) and its fitted trend (dotted) along the solid line in Fig. 5. *Right panel:* Wavelet transform of the trend-removed intensity profile. The white dashed line signifies the period (~ 192 s) with maximum power.

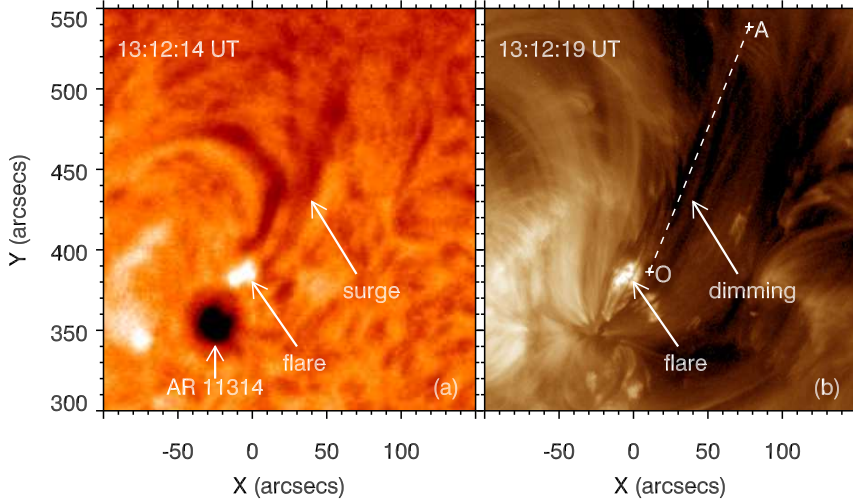


Fig. 7. *Left panel:* $H\alpha$ image at 13:12:14 UT featuring the AR 11314, flare, and cool surge as pointed by the white arrows. *Right panel:* AIA 193 Å image at 13:12:19 UT featuring the flare and dimming following the leading edge of jet as pointed by the white arrows. The dashed line (“OA”) is used for measuring the true height of jet.

we discovered magnetic cancellation before the flare. The temporal evolutions of magnetic flux of the three regions are demonstrated in Fig. 9 where Φ_{P1} , Φ_{P2} , and Φ_N represent the total positive magnetic flux of “P1”, positive flux of “P2”, and negative flux of “N”. It is evident that all the three polarities underwent continuous cancellation with small-scale fluctuations before the onset of jet and flare impulsive phase at 12:38 UT. Using linear curve-fitting, we derived the cancellation rate for the three polarities, being $d\Phi_{P1}/dt = -1.1 \times 10^{17}$ Mx hr $^{-1}$, $d\Phi_{P2}/dt = -4.6 \times 10^{16}$ Mx hr $^{-1}$, and $d\Phi_N/dt = -8.0 \times 10^{17}$ Mx hr $^{-1}$, respectively. The magnetic fluxes of “P2” and “N” kept on cancelling after the flare, while the flux of “P1” fluctuated and kept near-constant. The

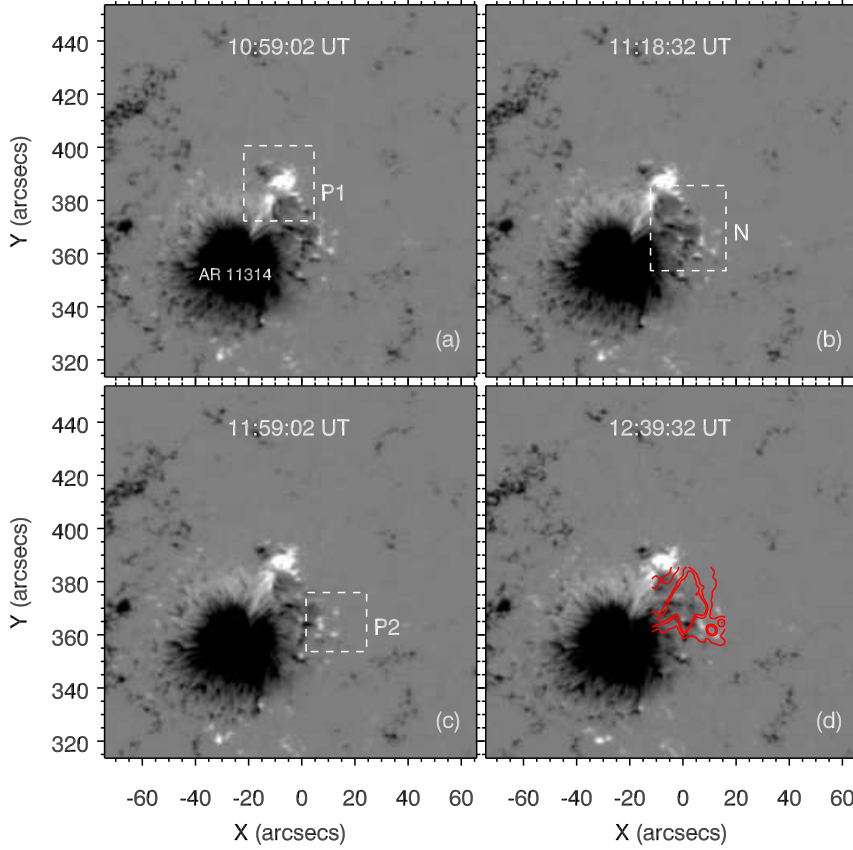


Fig. 8. HMI LOS magnetograms at 10:59:02 UT **(a)**, 11:18:32 UT **(b)**, 11:59:02 UT **(c)**, and 12:39:32 UT **(d)**. “P1” and “P2” with positive polarity are included by the white dashed boxes in panels **(a)** and **(c)**. “N” with negative polarity is included by the white dashed box in panel **(b)**. The red lines in panel **(d)** represent the intensity contour of flare shown in the top-left panel of Fig. 10.

observations of jets and surges as a result of flux emergence and cancellation have been reported (Liu & Kurokawa 2004; Jiang et al. 2007; Chifor et al. 2008).

To derive the 3D magnetic configuration of the flare-related jet, we performed potential-field extrapolation. In the top-left panel of Fig. 10, we show the AIA 193 Å image at 12:39:31 UT superposed by the HMI magnetogram contours at the same time where red/blue lines stand for positive/negative polarities. It features the bright compact flare and jet in the north-west direction. In the bottom-left panel of Fig. 10, we display the top-view of magnetic configuration, where grayscale image represents the magnetogram and the red/blue lines denote the closed/open magnetic field lines. It is obvious that the jet direction is well consistent with the orientation of projected open field lines.

In the top-right panel of Fig. 10, we display the EUVI running-difference image at 12:46:27 UT in 195 Å. Only the top segment of jet was observed while the lower segment of jet and flare were blocked. The included angle between the jet and the projection of plane-of-the-sky on the EUVI image (dashed line) is denoted with θ that measures 11.3° . In the bottom-right panel of Fig. 10,

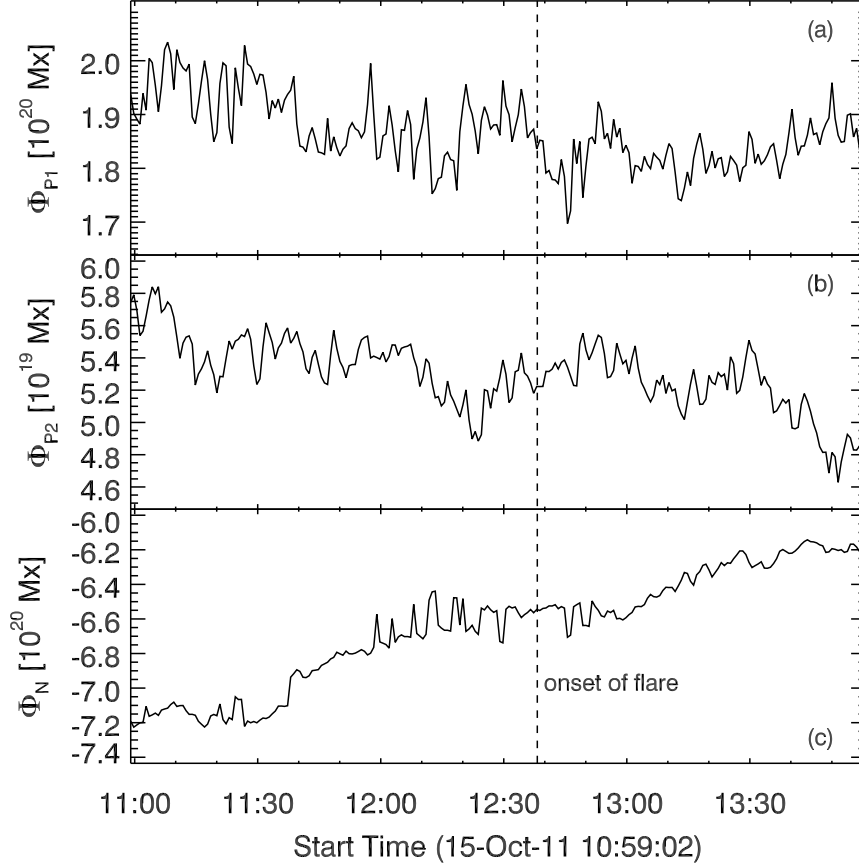


Fig. 9. Temporal evolutions of the magnetic fluxes of “P1” (a), “P2” (b), and “N” (c). The dashed line denotes the start of jet and flare impulsive phase.

we demonstrate the side-view of the magnetic field lines from STEREO-B viewpoint. It is obvious that the direction of jet is also consistent with the direction of open fields.

Since we have two perspectives to view the flare-related jet, one is from SDO/AIA, the other is from STEREO-B/EUVI, we can take the projection effect into account to estimate the true height and speed. In the right panel of Fig. 7, we label the bottom and leading edge of jet with “O” and “A”, whose distance equals to the apparent height of jet, i.e., 120.7 Mm. Considering the angular derivation (θ) of jet from plane-of-the-sky, the true height and initial velocity are estimated to be 122.7 Mm and $258 \pm 10 \text{ km s}^{-1}$.

4. Discussion and summary

The rising and subsequent falling of jets and surges along their axis have been extensively reported. Roy (1973) found that the acceleration of falling material of $H\alpha$ surges was less than the solar free fall acceleration (g_\odot). Liu et al. (2009) found that the effective gravitational acceleration of the Ca II H jet had a mean value of 141 m s^{-2} . Shen et al. (2011) discovered an even smaller value (26 m s^{-2}) that was interpreted by the projection effect or damping effect of the background magnetic fields. For our case, the parallel gravitational acceleration (g_{\parallel}) accounts for $\frac{1}{3}g_\odot - \frac{1}{2}g_\odot$ in the solar atmosphere. We propose that the Lorentz force of twisted jet threads (“T1” and “T2” in Fig. 1b) serves as an upward force against gravity.

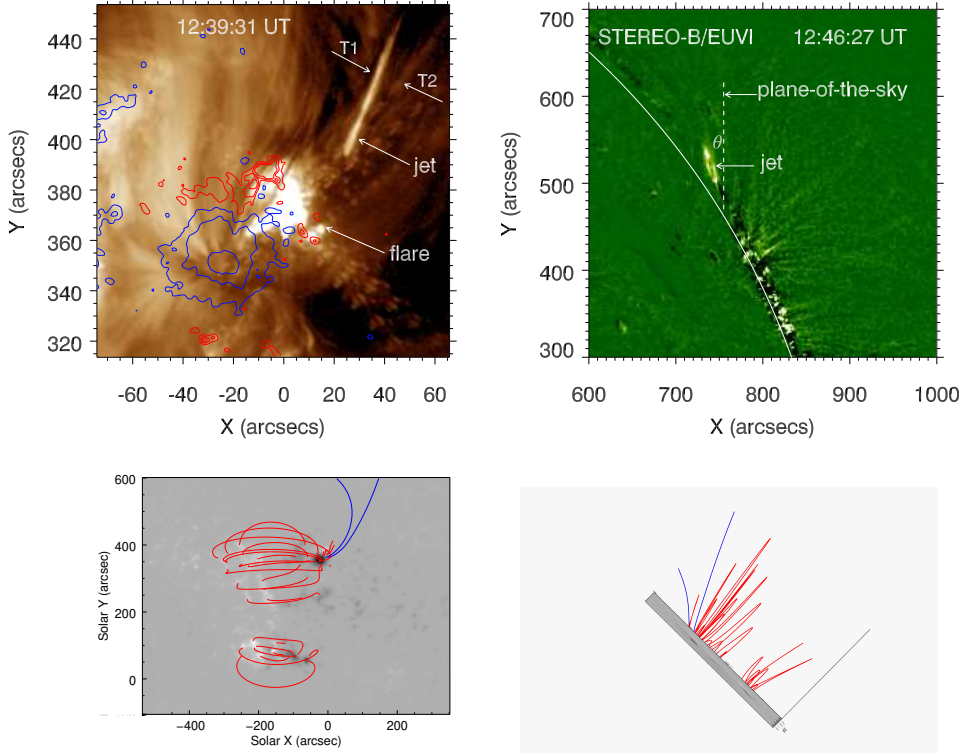


Fig. 10. *Top left:* AIA 193 Å image at 12:39:31 UT that features the jet threads (“T1” and “T2”) and flare as pointed by the white arrows. The red/blue lines stand for the contours of positive and negative polarities of the HMI LOS magnetogram at 12:39:32 UT. *Top right:* Running-difference image of STEREO-B/EUVI in 195 Å at 12:46:27 UT, showing the top segment of jet. The dashed line stands for the projection of plane-of-the-sky on the EUV image. The included angle between the jet and plane-of-the-sky is labeled with θ . *Bottom panels:* Top-view (*left*) and side-view (*right*) of the 3D magnetic field lines. The red/blue lines represent closed/open magnetic field lines.

Coronal mass ejections (CMEs; Chen 2011; Cheng et al. 2011) are often accompanied by EUV waves and the following dimming that was interpreted by density depletion (Chen et al. 2002, 2010). Such dimmings accompanying EUV jets have rarely been reported. Shen et al. (2011) observed a cavity obvious in 304 Å but undetectable in 193 Å, suggesting the cool temperature of cavity. Lee et al. (2013) discovered a fast jet-associated EUV dimming that is explained by Alfvénic waves initiated by reconnection in the upper chromosphere. In our study, the dimming following the leading edge of jet was detectable in all the EUV passbands of AIA. The appearance/disappearance of dimming coincided with the longitudinal rising/falling motions of jet. It is revealed in Fig. 7 that the dimming is cospatial with the $H\alpha$ surge, indicating that the dimming resulted from the absorption of hot EUV emission by the cool surge. The disappearance of surge at $\sim 13:18$ UT coincided with the disappearance of dimming around 13:20 UT. Yokoyama & Shibata (1996) performed MHD numerical simulations to explain the generation of hot jet and cool surge during the magnetic reconnection between the emerging magnetic flux and the pre-existing fields of opposite polarity. The jet and surge are adjacent in the 2D simulation. However, if we observe the eruption from an appropriate viewpoint, the jet would be blocked by the foreground surge, leading to the absorption of EUV emission by the $H\alpha$ surge at a lower speed.

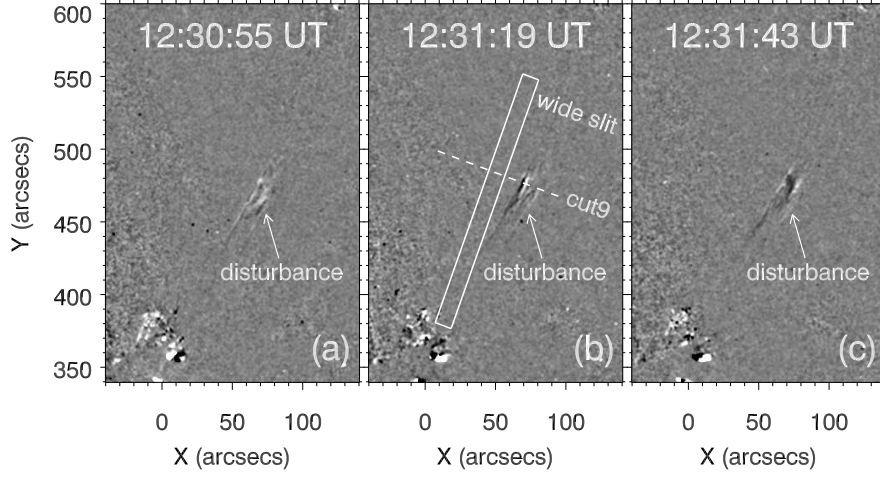


Fig. 11. Running-difference images in 193 \AA during 12:30–12:32 UT. White/black color denotes intensity increase/decrease. The arrows point to the transverse disturbances adjacent to the jet axis prior to the flare.

The helical structure and untwisting motions of EUV jets have been extensively investigated since the launch of high-resolution space telescopes (e.g., SDO). Such motions were often explained by the releasing of accumulated magnetic helicity into the upper solar atmosphere. The jet we observed underwent counter-clockwise rotation at the beginning of its eruption. The transverse velocities range from 40 to 200 km s^{-1} , very close to the values reported by Shen et al. (2011). The rotation slowed down from $\sim 122 \text{ km s}^{-1}$ in the initial phase to $\sim 80 \text{ km s}^{-1}$ in the later phase, which is in agreement with the cases of Liu et al. (2009) and Schmieder et al. (2013). The rotation, however, lasted for only 1 cycle with period of ~ 7 min, which is in the same order of magnitude as the previously reported values (Liu et al. 2009; Chen et al. 2012).

Precursor disturbances before the transverse jet rotation were observed. Figure 11 shows the running-difference images during 12:30–12:32 UT in 193 \AA , where white/black color represents intensity increase/decrease. Transverse disturbances adjacent to the jet axis are distinguishable in the images. In the time-slice diagram of cut9 (third row of Fig. 3), we label the disturbances with four dotted lines, the slope of which represent the velocities, being $-175, 126, -24, 51 \text{ km s}^{-1}$, respectively. As to the cause of the disturbances, we noticed weak brightenings during 12:30–12:36 UT before the impulsive phase of flare in the $0.4\text{--}5.0 \text{ \AA}$ light curve (Fig. 1d). Precursor brightenings, implying small-scale and weak release of magnetic energy prior to the impulsive phase of flares, have been observed (Harrison et al. 1985; Chifor et al. 2007), and are consistent with the mechanism of blowout jets (Moore et al. 2010).

In this paper, we report a flare-related jet observed by SDO/AIA on 2011 October 15. The jet underwent longitudinal rising/falling along its axis with an initial velocity of $254 \pm 10 \text{ km s}^{-1}$. The effective gravitational acceleration was $-97 \pm 5 \text{ m s}^{-2}$, well below the free fall acceleration. The onset of jet eruption coincided with the beginning of impulsive phase of the adjacent C1.6 flare. At the beginning of its longitudinal eruption, the jet presented helical structure and counter-clockwise swirling motion that slowed down from an average of $\sim 122 \text{ km s}^{-1}$ in the initial stage to $\sim 80 \text{ km s}^{-1}$ in the later stage. The thick interwinding threads of jet untwisted into multiple thin threads during the rotation that lasted for only 1 cycle with period of ~ 7 min and amplitude that

increases from ~ 3.2 Mm at the lower part to ~ 11 Mm at the upper part. Afterwards, a dimming region appeared following the curtain-like leading edge of jet. The appearance/disappearance of dimming coincided with the ascending/descending motions. The cospatial EUV dimming and $H\alpha$ surge indicate that the dimming resulted from the absorption of hot EUV emission by the cool surge. LOS magnetograms from SDO/HMI show that the flare/jet event was caused by continuous magnetic cancellation before the eruption. Potential-field extrapolation based on the magnetograms reveals that the jet was associated with the open magnetic fields at the boundary of AR 11314. The true height and velocity of jet were estimated after considering the projection effect from the two perspectives of SDO and STEREO-B.

Acknowledgements. The authors are grateful to the referee for enlightening comments. Q.M.Z acknowledges J. Q. Sun, P. F. Chen, Y. Guo, R. Erdélyi, G. Verth, Y. N. Su, and the solar physics group in Purple Mountain Observatory for valuable discussions and suggestions. Q.M.Z is also thankful for the Department of Applied Mathematics in the University of Sheffield for their hospitality during his visit. SDO is a mission of NASA's Living With a Star Program. AIA and HMI data are courtesy of the NASA/SDO science teams. STEREO/SECCHI data are provided by a consortium of US, UK, Germany, Belgium, and France. The Global Oscillation Network Group (GONG) Program is managed by the National Solar Observatory. This work is supported by 973 program under grant 2011CB811402 and by NSFC 11303101, 11333009, 11173062 and 11221063.

References

- Canfield, R. C., Reardon, K. P., Leka, K. D., et al. 1996, *ApJ*, 464, 1016
- Chae, J., Qiu, J., Wang, H., & Goode, P. R. 1999, *ApJ*, 513, L75
- Chen, F., Ding, M. D., & Chen, P. F. 2010, *ApJ*, 720, 1254
- Chen, H. D., Zhang, J., & Ma, S. L. 2012, *Research in Astronomy and Astrophysics*, 12, 573
- Chen, P. F. 2011, *Living Reviews in Solar Physics*, 8, 1
- Chen, P. F., Wu, S. T., Shibata, K., & Fang, C. 2002, *ApJ*, 572, L99
- Cheng, X., Zhang, J., Liu, Y., & Ding, M. D. 2011, *ApJ*, 732, L25
- Chifor, C., Tripathi, D., Mason, H. E., & Dennis, B. R. 2007, *A&A*, 472, 967
- Chifor, C., Isobe, H., Mason, H. E., et al. 2008, *A&A*, 491, 279
- Cirtain, J. W., Golub, L., Lundquist, L., et al. 2007, *Science*, 318, 1580
- Culhane, L., Harra, L. K., Baker, D., et al. 2007, *PASJ*, 59, 751
- De Pontieu, B., Erdélyi, R., & James, S. P. 2004, *Nature*, 430, 536
- Glesener, L., Krucker, S., & Lin, R. P. 2012, *ApJ*, 754, 9
- Guo, Y., Démoulin, P., Schmieder, B., et al. 2013, *A&A*, 555, A19
- Harrison, R. A., Waggett, P. W., Bentley, R. D., et al. 1985, *Sol. Phys.*, 97, 387
- Hong, J.-C., Jiang, Y.-C., Yang, J.-Y., et al. 2013, *Research in Astronomy and Astrophysics*, 13, 253
- Howard, R. A., Moses, J. D., Vourlidas, A., et al. 2008, *Space Sci. Rev.*, 136, 67
- Ji, H., Wang, H., Liu, C., & Dennis, B. R. 2008, *ApJ*, 680, 734
- Jiang, R.-L., Fang, C., & Chen, P.-F. 2012, *ApJ*, 751, 152
- Jiang, Y. C., Chen, H. D., Li, K. J., Shen, Y. D., & Yang, L. H. 2007, *A&A*, 469, 331
- Jibben, P., & Canfield, R. C. 2004, *ApJ*, 610, 1129
- Kaiser, M. L. 2005, *Advances in Space Research*, 36, 1483
- Kim, Y.-H., Moon, Y.-J., Park, Y.-D., et al. 2007, *PASJ*, 59, 763
- Krucker, S., Kontar, E. P., Christe, S., Glesener, L., & Lin, R. P. 2011, *ApJ*, 742, 82
- Lee, K.-S., Innes, D. E., Moon, Y.-J., et al. 2013, *ApJ*, 766, 1
- Lemen, J. R., Title, A. M., Akin, D. J., et al. 2012, *Sol. Phys.*, 275, 17
- Liu, C., Deng, N., Liu, R., et al. 2011a, *ApJ*, 735, L18
- Liu, W., Berger, T. E., Title, A. M., & Tarbell, T. D. 2009, *ApJ*, 707, L37
- Liu, W., Berger, T. E., Title, A. M., Tarbell, T. D., & Low, B. C. 2011b, *ApJ*, 728, 103
- Liu, Y., & Kurokawa, H. 2004, *ApJ*, 610, 1136

- Moore, R. L., Cirtain, J. W., Sterling, A. C., & Falconer, D. A. 2010, *ApJ*, 720, 757
- Moreno-Insertis, F., Galsgaard, K., & Ugarte-Urra, I. 2008, *ApJ*, 673, L211
- Moreno-Insertis, F., & Galsgaard, K. 2013, *ApJ*, 771, 20
- Moschou, S. P., Tsinganos, K., Vourlidas, A., & Archontis, V. 2012, *Sol. Phys.*, 310
- Nishizuka, N., Shimizu, M., Nakamura, T., et al. 2008, *ApJ*, 683, L83
- Nisticò, G., Bothmer, V., Patsourakos, S., & Zimbardo, G. 2009, *Sol. Phys.*, 259, 87
- Pariat, E., Antiochos, S. K., & DeVore, C. R. 2009, *ApJ*, 691, 61
- Pariat, E., Antiochos, S. K., & DeVore, C. R. 2010, *ApJ*, 714, 1762
- Patsourakos, S., Pariat, E., Vourlidas, A., Antiochos, S. K., & Wuelsel, J. P. 2008, *ApJ*, 680, L73
- Pontin, D. I., Priest, E. R., & Galsgaard, K. 2013, *ApJ*, 774, 154
- Roy, J.-R. 1973, *Sol. Phys.*, 32, 139
- Savcheva, A., Cirtain, J., Deluca, E. E., et al. 2007, *PASJ*, 59, 771
- Scherrer, P. H., Schou, J., Bush, R. I., et al. 2012, *Sol. Phys.*, 275, 207
- Schmieder, B., Shibata, K., van Driel-Gesztelyi, L., & Freeland, S. 1995, *Sol. Phys.*, 156, 245
- Schmieder, B., Guo, Y., Moreno-Insertis, F., et al. 2013, *A&A*, 559, A1
- Shen, Y., Liu, Y., Su, J., & Ibrahim, A. 2011, *ApJ*, 735, L43
- Shibata, K., & Uchida, Y. 1986, *Sol. Phys.*, 103, 299
- Shibata, K., Ishido, Y., Acton, L. W., et al. 1992, *PASJ*, 44, L173
- Shibata, K., Nakamura, T., Matsumoto, T., et al. 2007, *Science*, 318, 1591
- Shimojo, M., Hashimoto, S., Shibata, K., et al. 1996, *PASJ*, 48, 123
- Singh, K. A. P., Isobe, H., Nishizuka, N., Nishida, K., & Shibata, K. 2012, *ApJ*, 759, 33
- Török, T., Aulanier, G., Schmieder, B., Reeves, K. K., & Golub, L. 2009, *ApJ*, 704, 485
- Wang, Y.-M., Sheeley, N. R., Jr., Socker, D. G., et al. 1998, *ApJ*, 508, 899
- Yokoyama, T., & Shibata, K. 1996, *PASJ*, 48, 353
- Zhang, J., Wang, J., & Liu, Y. 2000, *A&A*, 361, 759
- Zhang, Q. M., Chen, P. F., Guo, Y., Fang, C., & Ding, M. D. 2012, *ApJ*, 746, 19
- Zhang, Q. M., & Ji, H. S. 2013, *A&A*, 557, L5